The diffusion-driven orthorhombic to tetragonal transition in YBa2Cu3O7 derived with a machine learning interatomic potential

Original
The diffusion-driven orthorhombic to tetragonal transition in YBa2Cu3O7 derived with a machine learning interatomic potential / Gambino, D., Di Eugenio, N., Byggmästar, J., Klarbring, J., Torsello, D., Djurabekova, F., Laviano, F.. - In: NPJ QUANTUM MATERIALS. - ISSN 2397-4648. - 11:1(2026), pp. 1-9. [10.1038/s41535-026-00891-7]

Publisher:
Springer Nature

Published
DOI:10.1038/s41535-026-00891-7

npj | quantum materials

Published in partnership with Nanjing University

Article

https://doi.org/10.1038/s41535-026-00891-7

The diffusion-driven orthorhombic to tetragonal transition in $YBa_2Cu_3O_7$ derived with a machine learning interatomic potential

Davide Gambino[1,2] ✉, Niccolò Di Eugenio[3,4], Jesper Byggmästar[2], Johan Klarbring[1], Daniele Torsello[3,4], Flyura Djurabekova[2,5] & Francesco Laviano[3,4]

Defects in high-temperature superconductors such as $YBa_2Cu_3O_7$ (YBCO) critically influence their superconducting behavior, as they substantially degrade or even suppress superconductivity. With the renewed interest in cuprates for next-generation superconducting magnets operating in radiation-harsh environments such as fusion reactors and particle accelerators, accurate atomistic modeling of defects and their dynamics has become essential. Here, we present a general-purpose machine-learning interatomic potential for YBCO, based on the Atomic Cluster Expansion (ACE) method and trained on density functional theory (DFT) data, with particular emphasis on defects and their diffusion mechanisms. The potential is validated against DFT calculations of ground-state properties, defect formation energies of oxygen Frenkel pairs, and diffusion barriers for their formation. Remarkably, the potential captures the diffusion-driven orthorhombic to tetragonal transition at elevated temperatures, a transformation that is difficult to describe with empirical potentials, elucidating how the formation of oxygen Frenkel pairs in the basal plane governs this order-disorder transition. The ACE potential introduced here enables large-scale, predictive atomistic simulations of defect dynamics and transport processes in YBCO, providing a powerful tool to explore its stability, performance, and functionality under realistic operating conditions. Moreover, this work proves that machine learning interatomic potentials are suitable for studies of quaternary oxides with complex chemistry.

Rare-earth barium cuprates (REBCOs) are subject to renewed interest[1] following recent technological developments in the fabrication of high-temperature superconducting (HTS) tapes[2,3] and their proposed employment in compact[4–8] and standard fusion reactors[9,10], as well as particle accelerators[11–13]. Together with recent advances in the fields of synchrotron radiation and ptychography[14–19], this renewed focus is likely to stimulate further progress in the fundamental understanding of these materials.

Since their discovery[20], REBCOs have proven to be extremely challenging materials to investigate both experimentally and theoretically. The coupling mechanism driving superconductivity in these materials remains debated[21–28], and all their properties are intimately linked with the stoichiometry of the oxygen sublattice. In $YBa_2Cu_3O_{7-x}$ (YBCO), for example, varying x drives the system from an antiferromagnetic insulator ($x \approx 1$) to a strange metal/superconductor ($x \approx 0$)[29]. In addition, the synthesis of REBCOs is plagued by defects: single crystals of these materials are difficult to produce and are characterized by the presence of extended defects such as twin boundaries[30] and a certain degree of disorder in the oxygen sublattice[31], with beneficial (vortex pinning) and detrimental (Cooper pair scattering) effects depending on the type of defect[32–36]. Oxygen vacancies in the CuO chains in the basal plane are known to introduce holes in the CuO_2 planes[37], and their amount governs the superconducting critical properties[38]. Indeed, it is observed that annealing of irradiated samples partly recovers the pristine critical superconducting properties even at cryogenic temperatures[39–42], strongly indicating that the O defect diffusion and recombination is an

---

[1]Department of Physics, Chemistry, and Biology (IFM), Linköping University, Linköping, SE-58183, Sweden. [2]Department of Physics, University of Helsinki, P.O. Box 43, Helsinki, FI-00014, Finland. [3]Department of Applied Science and Technology, Politecnico di Torino, Corso Duca degli Abruzzi, 24, Torino, I-10129, Italy. [4]Istituto Nazionale di Fisica Nucleare (INFN), Sezione di Torino, Via P. Giuria, 1, Torino, I-10125, Italy. [5]Helsinki Institute of Physics (HIP), P.O.Box 64, Helsinki, FI-00014, Finland.
✉e-mail: davide.gambino@liu.se

extremely important effect in these materials[43]. Detailed understanding of the defect formation process is of utmost importance for technological applications in radiation-harsh environments, and the impact of different types of defects on the superconducting properties should be understood to improve HTS device design[44]. Because of experimental limitations in reproducing operational conditions of, e.g., fusion reactors[45], computational modeling with first principles and atomistic methods can guide the development of devices by giving insights into the microscopic mechanisms of degradation and possible recovery mechanisms[46].

Disorder in the oxygen sublattice is also responsible for the orthorhombic to tetragonal transition occurring at high temperatures over a broad range of stoichiometries[47–49]. Neutron diffraction studies of YBCO[47,48] have shown that the mechanism governing this transition consists of a rearrangement of the occupation of the O sites in the basal plane, with O atoms from the CuO chains moving to the available sites in between the chains. This disorder in the basal plane leads to a lack of preferential direction in the *a* and *b* directions, driving the transition to a higher-symmetry crystal structure.

The orthorhombic-to-tetragonal transition has also been observed in molecular dynamics (MD) simulations by Chaplot[50], using a simple interatomic potential specifically tuned to reproduce the experimental transition temperature[50–52]. A more general classical interatomic potential was later developed by Gray et al.[53] for studying radiation damage and defect properties[45,53,54]. This potential combines Buckingham and Coulomb terms, with parameters fitted to density functional theory (DFT) data; however, it exhibits some limitations, for instance, it employs fixed charges, which require overall neutrality in the system.

Machine learning potentials (MLPs)[55–58] trained on DFT calculations offer a powerful route to overcome such limitations. However, specialized MLPs for systems with many elements and complex chemistry are quite rare[59–61], and even further challenges are introduced by the modeling of defects[62–66]. YBCO, with its large unit cell, many inequivalent atomic sites, and its diffusion-driven, order-disorder structural transition, provides a challenging testbed for assessing the capabilities of MLPs to describe diverse bonding in the same compound and defect dynamics. In this work, we develop an MLP based on the Atomic Cluster Expansion (ACE) method[67,68] trained on DFT data, including defects of all species. The ACE potential improves upon the classical potential of Gray et el.[53] across a wide range of properties and, crucially, reproduces the orthorhombic-to-tetragonal transition at elevated temperatures. Our simulations reveal that this transition is entropy-driven, facilitated by the decreasing formation energy of oxygen Frenkel pairs (FPs) in the basal plane due to thermal expansion. Our results demonstrate the capability of MLPs to capture complex defect physics in quaternary oxide compounds, paving the way for predictive simulations of their behavior under radiation-harsh conditions.

Results

DFT reference data set and training of the ACE potential

The training dataset was constructed to capture both equilibrium and non-equilibrium environments relevant to defect formation and diffusion in YBCO. Configurations were first generated from MD simulations (416 atoms) over a wide temperature range for the defect-free structure and for structures containing all possible vacancies and interstitials, using a preliminary ACE potential trained on low-accuracy ab initio MD and defect relaxations taken from ref. 41. Additional defect-free structures over a broad range of volumes from DFT relaxations were included, spanning compressed to highly expanded lattices. To ensure representation of disordered states, we also incorporated manually generated amorphous-like configurations (52 atoms) that exhibit liquid-like local environments. To better target the orthorhombic-to-tetragonal transition, the dataset was enriched with perturbed structures containing oxygen FPs (vacancies at each inequivalent oxygen site combined with oxygen interstitials at the O5 site; see Fig. 1), as well as approximate transition-state (TS) geometries for FP formation. The diversity of these configurations, summarized visually in Fig. 1, ensures balanced coverage of the relevant defect physics and structural transitions. The data set is composed of 1368 configurations (545,267 atoms) in total, see Supplementary Table I for further details.

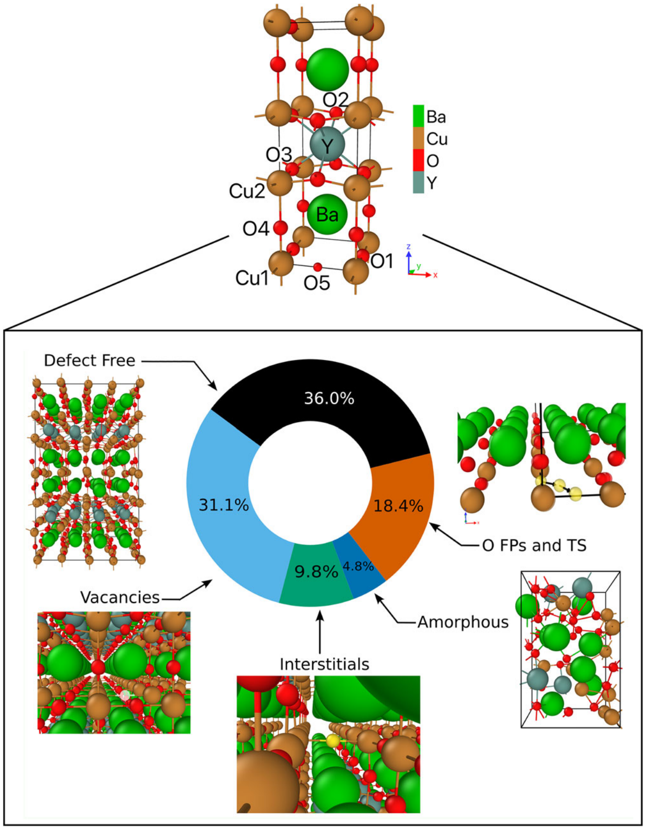

Fig. 1 | Composition of the dataset. Unit cell of YBCO with its inequivalent crystallographic positions and the most stable interstitial position for O atoms (O5 position), and a visual representation of the dataset with example structural models generated with OVITO[70]. Y, Ba, Cu, and O are in teal, green, brown, and red colors, respectively.

As shown in the parity plots (Fig. 2), the potential achieves high accuracy for both energies and forces, with RMSEs of 10 meV/atom and 70 meV/Å, respectively, on both the training and test sets (the latter comprising 5% of the full dataset, randomly selected). A small set of off-diagonal points in Fig. 2b was traced to a DFT artifact arising during fixed-volume relaxation of the ideal structure. After recalculating the problematic configuration, the ACE potential was found to predict energies and forces in much closer agreement with the corrected DFT values (≈4 meV/atom for energies and ≤15 meV/Å for forces). This demonstrates that the potential remains robust and accurate, even in the presence of such a problematic configuration in the training set.

Validation of the ACE potential

To validate the accuracy of the developed potential, we calculated the equation of state for YBCO using our ACE potential and compared it with results from DFT and the Buckingham + Coulomb (B + C) classical potential of Gray et al.[53] (Fig. 3a). Both the ACE and the B + C potentials closely reproduce the DFT results, although the B + C curve has been shifted vertically here to match the minimum with the DFT results. The superiority of the ACE potential becomes apparent when examining the *a*, *b*, and *c* lattice parameters (Fig. 3b–d): ACE accurately captures the slope of all lattice parameters around equilibrium and closely follows the non-monotonic trend at large volumes observed in DFT. In contrast, the B + C potential overestimates the slope of the *a* lattice parameter, underestimates that of the *c* parameter, and fails to reproduce the large-volume behavior. This failure of the B + C potential is probably due to the lack of flexibility of this model, inherited from the fixed charges assigned to each

Fig. 2 | Statistical analysis of training. a, **b** Parity plots of training and **c**, **d** test sets of energies (**a**, **c**) and forces (**b**, **d**), with each subset represented with different colors (defect-free: black; vacancies: light blue; interstitials: green; amorphous: dark blue; oxygen Frenkel pairs and transition states (O FPs and TS): orange). RMSEs are 10.8 meV/atom and 69.0 meV/Å on energy and forces from the training set, and 9.4 meV/atom and 68.9 meV/Å from the test set.

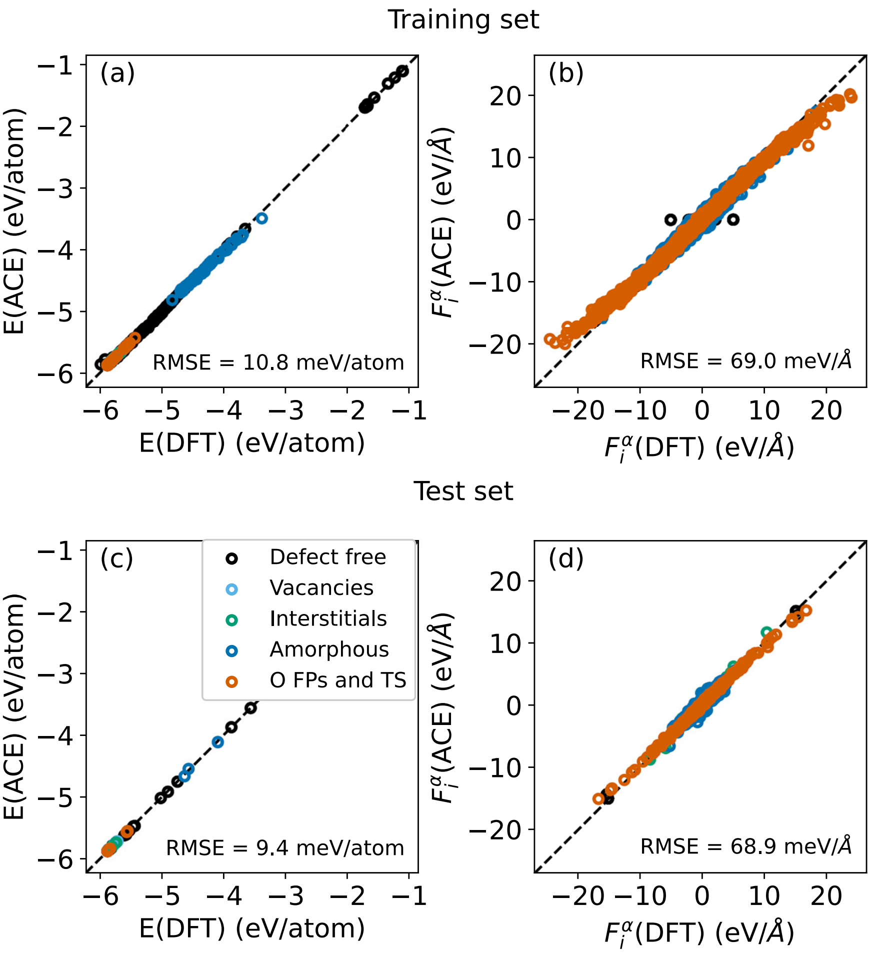

Fig. 3 | Energy and lattice parameters as a function of volume. a Equation of state of YBCO from DFT (blue empty circles), the Buckingham + Coulomb potential (B + C, green dashed line), and the ACE potential (yellow solid line). The B + C equation of state curve has been rigidly shifted vertically to match the DFT minimum energy. **b**–**d** Lattice parameters *a*, *b*, and *c* as a function of volume at 0 K from DFT, B + C, and ACE.

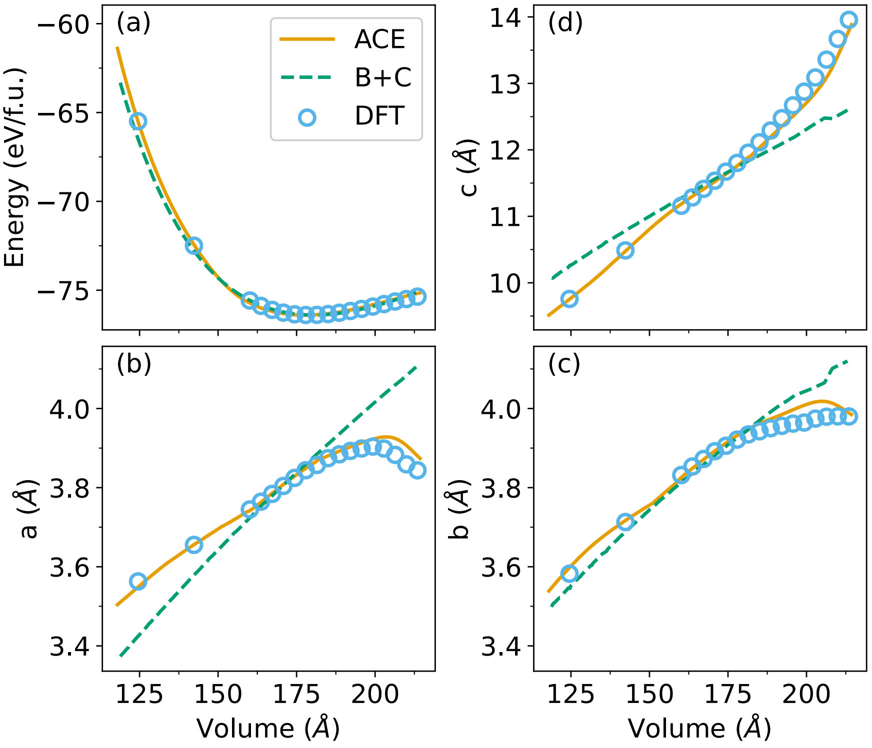

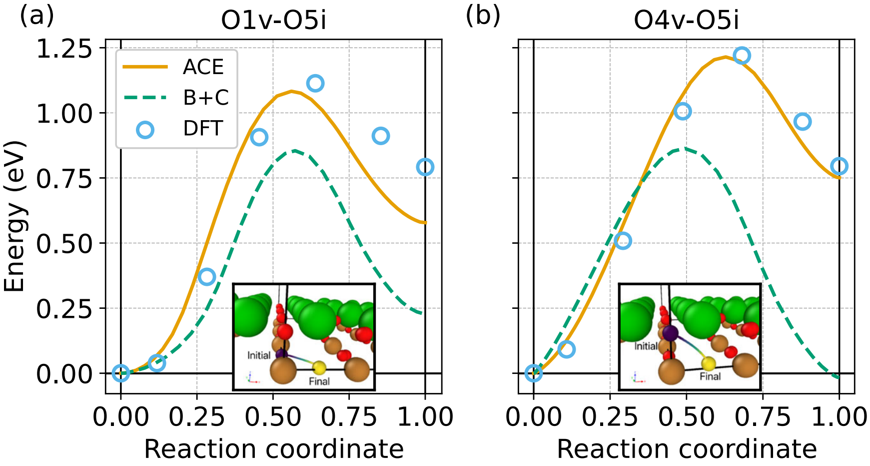

Fig. 4 | O FPs formation energy barriers. a Energy barrier for the formation of the oxygen FP O1v-O5i from DFT (blue empty circles), ACE (yellow solid line), and the B + C potential (green dashed line). The final energy corresponds to the formation energy of the FP. The figure inset shows the migration path within the YBCO cell, with the migrating atom going from initial (dark violet) to final (yellow) position. **b** The same for the oxygen FP O4v-O5i.

species. ACE is able to capture local rearrangements occurring at volumes far from equilibrium, demonstrating its ability to reproduce the physical behavior of this challenging system.

We further validated the potential on defect energetics relevant to the orthorhombic-to-tetragonal transition, focusing on FPs formed by diffusion of oxygen from the O1 and O4 sites to the O5 site (see Fig. 4). The ACE potential reproduces the migration energies of both processes with high accuracy, within 20 meV of the DFT reference, substantially improving upon the B + C potential, which underestimates these barriers by 0.3–0.4 eV. Formation energies are similarly well captured: for O4v-O5i, ACE predicts 0.77 eV vs. 0.81 eV from DFT, while B+C incorrectly stabilizes this defect relative to the pristine structure. The O1v-O5i formation energy is slightly underestimated by ACE (0.62 vs. 0.79 eV from DFT), but remains significantly closer than B + C (≈0.5 eV below DFT). This defect is intrinsically difficult to reproduce, as the local oxygen coordination with its copper first nearest neighbors is nearly identical to the defect-free environment. Nonetheless, errors of ≈0.2 eV in defect formation energies are typical for MLPs[62–66], and the high accuracy in reproducing migration barriers underscores the reliability of the potential for the investigation of oxygen diffusion in YBCO. Additional validation on lattice dynamics, mechanical properties, and oxygen FPs energetics is shown in Supplementary Tables II and III, and Supplementary Figs. 1 and 2.

The orthorhombic to tetragonal transition

Capturing the orthorhombic to tetragonal transition in YBCO is particularly challenging for interatomic potentials, since it is driven by subtle diffusion processes and disorder in the oxygen sublattice. Here, we show that the ACE potential is able to reproduce this transition by carrying out NPT simulations over a wide temperature range (200–1400 K) with large simulation cells (≈25,000 atoms) up to 75 ns. The transition occurs spontaneously at approximately 800 K (see Fig. 5a), with signs of a disordered orthorhombic phase already at 700 K, in reasonable agreement with the experimental transition observed at 1000 K[47]. Although the simulations were run for unusually long times compared to typical MD studies, the structures at 700 and 750 K still exhibited incomplete convergence (see Supplementary Figs. 3 and 4 for details on the lattice parameters).

The transition can be identified as an order-disorder transition, in which the linearity of the CuO chains in the basal plane of the ordered, orthorhombic structure is progressively broken by migration of oxygen from the O1 sites to the O5 sites, leading to the tetragonal phase (Fig. 5d–h) where these sites are randomly occupied and the chains lose long-range order. The degree of disorder can be visually estimated by the length of the chains in the snapshots, with an apparent decrease in length with increasing temperature. In partially disordered structures Fig. 5f, g, it is clear that at 700 K chains are mostly in the *b* direction, whereas at 750 K this preference is already decreased, with longer chains forming in the *a* direction. At 1200 K, the chains do not show any preferential direction, with chains of similar length in both *a* and *b* directions. At the transition, we observe an occupancy of the O1 and O5 positions slightly higher than 0.5 atoms/f.u., where the additional oxygen atoms come from the O4 lattice position (see Fig. 5c). With increasing temperature, the occupancy of the O1 and O5 positions steadily increases and the O4 occupation conversely decreases.

Comparison of the computational transition temperature with experiments is complicated by oxygen degassing in the experimental samples. In our bulk simulations, which conserve the number of particles, the orthorhombic-to-tetragonal transition is observed at lower temperatures than in experiments, consistent with the lower O1v-O5i FP formation energy of the ACE potential as compared to the DFT reference. However, the onset of basal-plane disorder observed in the present simulations at 700 K closely matches the experimental onset of oxygen loss[47], indicating that the ACE potential accurately captures the temperatures at which oxygen diffusion becomes significant. This suggests that increased oxygen mobility below the transition might initially deplete more effectively the newly occupied O5 sites, maintaining the orthorhombic structure up to higher temperatures as compared to our model with a conserved number of particles, explaining part of the present underestimation of transition temperature.

In contrast to the more complex comparison with the experimental transition temperature, the difference observed in the *c* lattice parameter between theory and experiment can be unambiguously attributed to oxygen degassing. The sharper rise of *c* observed experimentally in the transition region (Fig. 5b) is due to the known increase of *c* with decreasing oxygen content[49], not accounted for in our simulations. A complete investigation of the interplay between oxygen stoichiometry and the structural transition would require a potential capable of handling variable oxygen content and simulations in the grand-canonical ensemble or with open surfaces, which is beyond the scope of this work.

Inspection of Fig. 5h suggests that the disordered state is not, in fact, completely random. To examine this more closely, we calculated the Warren–Cowley short-range order (SRO) parameter[69] for first-nearest-neighbor oxygen sites (O1–O5) and second-nearest neighbors (O1–O1 and O5–O5) as a function of temperature, as shown in Fig. 6a. At low temperatures, all O1 sites are occupied and all O5 sites are vacant, giving an SRO parameter of 1 for the first shell, consistent with ordering between occupied and vacant sites, and −1 for the second shell, consistent with clustering within the O1 and O5 sublattices, respectively. At 650 K, the SRO begins to decay toward 0 for both shells, although significant correlations persist even at the highest temperature, particularly for first-nearest neighbors. This residual correlation arises because a Cu atom in the basal plane typically has only two O neighbors, which constrains the configurational freedom and prevents truly random occupation of the O1 and O5 sites.

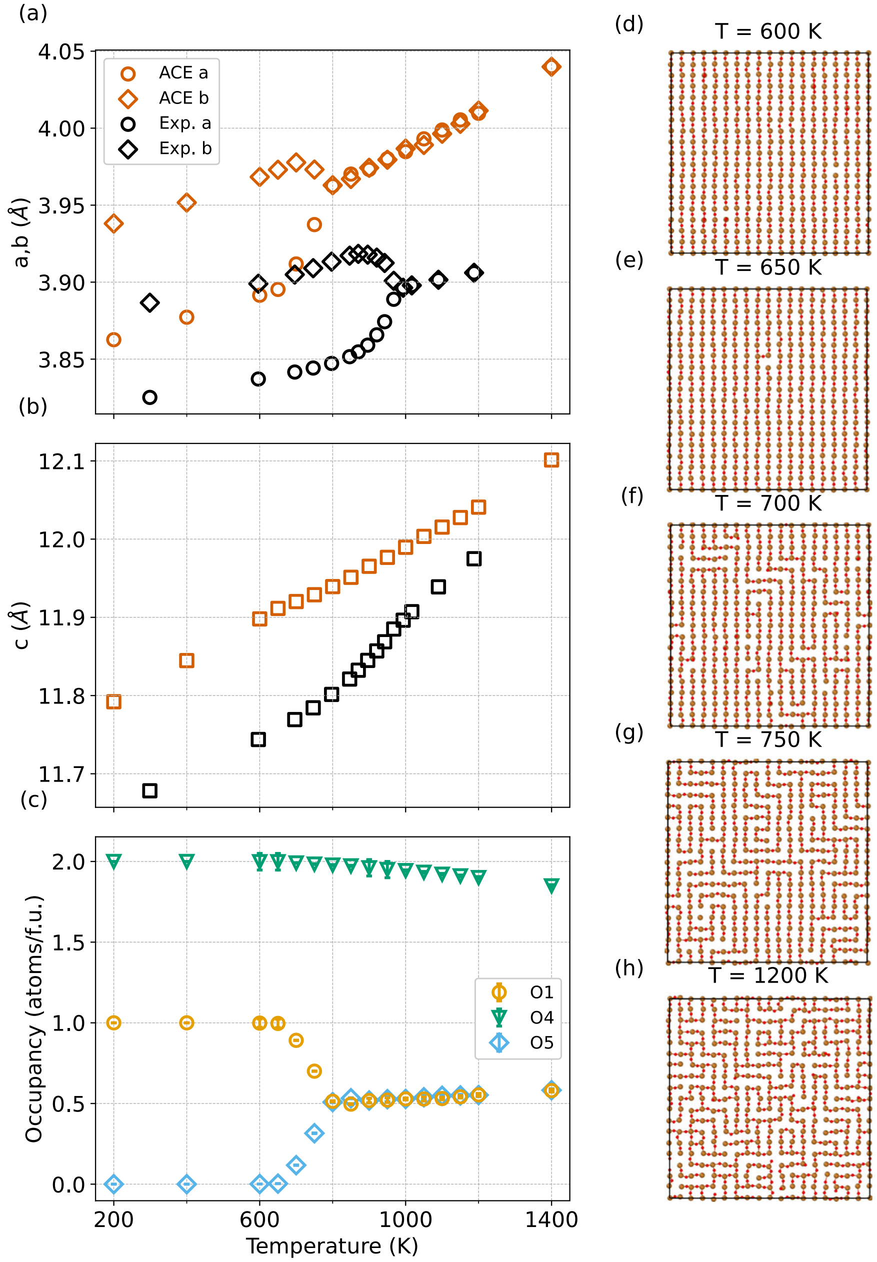

Fig. 5 | Orthorhombic to tetragonal transition as a function of temperature. a *a* (circles) and *b* (diamonds) lattice parameters as a function of temperature from ACE (orange) and experiments (black)[47]. **b** *c* lattice parameter as a function of temperature; **c** Occupation of O1, O4, and O5 sites as a function of temperature. **d**–**h** Snapshots of the basal plane progressing through the transition at temperatures of 600, 650, 700, 750, and 1200 K, respectively.

The hopping rate Γ of O atoms in the tetragonal phase is on the order of 10^{10}–10^{11} hops per second per oxygen atom and follows Arrhenius behavior, with an activation energy of 0.34 eV (see Fig. 6b). We define a hop as a change of site by an atom between two saved simulation frames. The frames are recorded every 1000 timesteps, and the sites are determined using the Wigner–Seitz analysis implemented in OVITO[70]. This elevated mobility with a low activation barrier is to be expected in the disordered phase, given the availability of vacant sites to jump in. It should be noted, however, that the present simulations were carried out in the NpT ensemble, and the thermostat may therefore influence the diffusion behavior of the atoms. Additional investigation is required to obtain deeper insight into the dynamics of YBCO.

To elucidate the thermodynamic origin of the order–disorder transition, we calculate the formation energy of the O1v-O5i FP at 0 K using the expanded lattice parameters obtained from NPT simulations and relaxing only atomic positions (see Fig. 6c). The formation energy decreases with expanding lattice parameters (i.e., increasing temperature), finding that it is energetically favorable to generate at least one FP for lattice parameters corresponding to temperatures of 1000 K or higher. Importantly, around 800 K, the system is already tetragonal, but the formation energy is positive, indicating that the formation of FPs is driven by entropic effects around the transition temperature rather than purely energetic ones. To verify the reliability of the ACE potential, we recalculated the formation energy with DFT at 3 different expanded lattices corresponding to 600, 1000, and 1400 K and observed a similar decrease in formation energy. The data point at 1400 K in Fig. 6c should be taken only as an indication of the trend in the formation energy, since the structure with one FP at this expanded lattice is not stable in DFT, with the interstitial atom inducing a heavy deformation of the neighboring CuO chains.

We also examined the effect of a small concentration of oxygen vacancies on the rate of transformation from the orthorhombic to the tetragonal phase. Simulations were performed at 800 and 1100 K with 2.5% and 5% vacancy concentrations in the O1 sublattice, and only minimal changes in the transition rate were observed. At 800 K, a small initial acceleration in the increase of the *a* lattice parameter is seen for the case with

Fig. 6 | Analysis of simulations and transition. **a** Short-range order (SRO) parameter of occupied and empty oxygen sites in the basal plane for first (blue) and second (yellow) nearest neighbors (NN1 and NN2, respectively). **b** Oxygen hopping rate (Γ) as a function of inverse temperature and its Arrhenius regression with fitted activation energy (E_a) of 0.34 eV. **c** Formation energy of the O1v-O5i FP (E^f(O1v-O5i)) at the expanded lattice parameters taken from the NPT simulations ($\{a, b, c\}_{eq}(T)$ indicates the equilibrium lattice vectors at temperature T). DFT is in blue full and empty circles, ACE is in yellow empty circles. The lines are a guide to the eye. The last DFT point is represented with an empty circle because the calculation did not converge (see text). **d** Running averages over 1.5 ns of the a (bottom curves) and b (top curves) lattice parameter as a function of time for 0 (black), 2.5 (blue), and 5 (yellow) % concentration of vacancies.

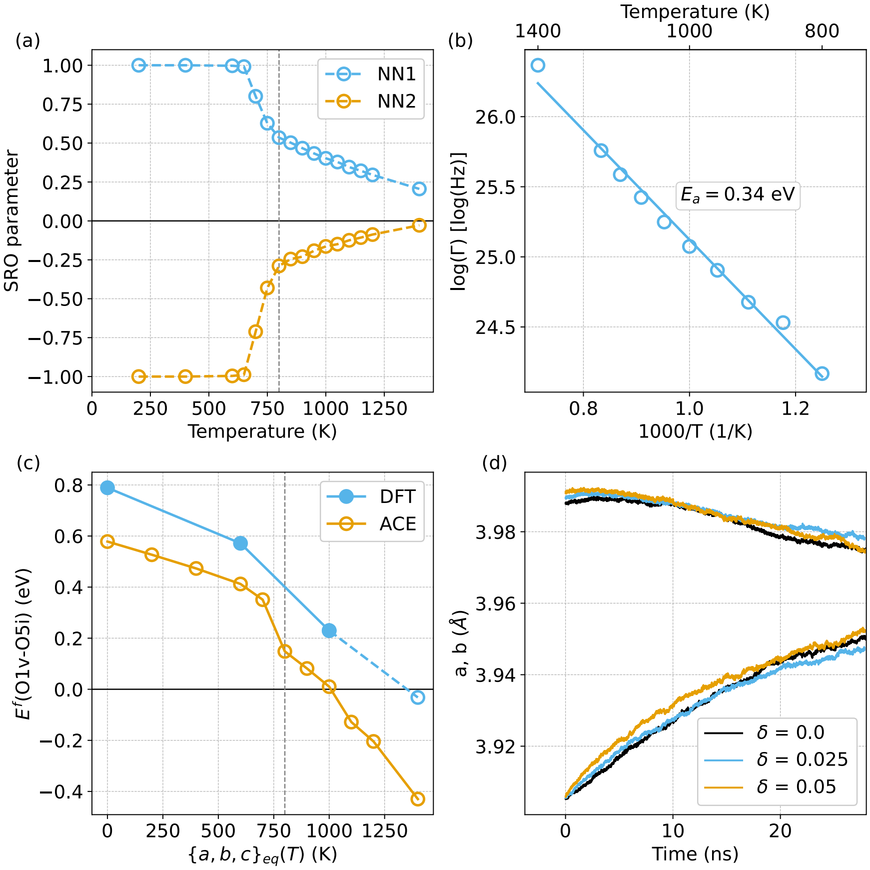

5% vacancies (see Fig. 6d), which may be consistent with experimental reports of a lower transition temperature at lower oxygen concentrations[47]. However, further work is required to investigate this dependence more carefully.

Discussion

In this work, we have developed an ACE potential for YBCO capable of describing the phase transition from the low-temperature orthorhombic structure to the high-temperature tetragonal structure. The potential has been validated against the equation of state, lattice parameters far from equilibrium, and oxygen FPs energetics.

We identify the mechanism driving the structural transition as the rearrangement of oxygen atoms in the basal plane: oxygen atoms from the CuO chains (O1) and, to a lesser extent, from the apical positions (O4) migrate to the interstitial O5 positions between the chains, effectively rendering the a and b directions equivalent. The transition is driven by entropic effects that favor disordering of the oxygen occupations in the basal plane, but it is facilitated by a reduced formation energy of oxygen FPs at expanded lattices.

The theoretical transition temperature is in reasonable agreement with experiments (800 K and approximately 1000 K, respectively), particularly considering that heating of YBCO is accompanied by oxygen loss, which effectively changes the chemistry of the system. Further progress will require extending the ACE potential to variable oxygen contents and employing advanced simulation techniques to access experimentally relevant timescales.

Overall, the developed potential enables the investigation of mass transport in this complex cuprate system with unprecedented accuracy. Beyond advancing our fundamental understanding of oxygen diffusion in HTS, this potential may also contribute to practical applications, such as optimizing annealing strategies for restoring superconductivity in radiation-damaged HTS tapes[40].

Methods

Dataset creation

The data set for defect-free structure, structures with single interstitials of each species, and structures with vacancies at each symmetrically inequivalent crystallographic position was created by taking snapshots from MD simulations carried out with a preliminary version of the potential. These simulations were run with $4 \times 4 \times 2$ supercells (416 atoms) at temperatures of 20, 250, 500, 750, 1000, and 1250 K.

To sample disordered environments, we included amorphous-like structures generated by randomly displacing the atoms in an ideal $2 \times 2 \times 1$ supercell according to a Gaussian distribution (0–8 Å), and wrapping the atoms back into the box. To avoid extreme overlap of atomic positions, these configurations were pre-relaxed for 10 steps with the purely repulsive Ziegler–Biersack–Littmark (ZBL) potential[71]. Subsequently, atomic positions were relaxed according to DFT forces for 10 ionic steps to reduce excessively high forces.

The oxygen FPs configurations included in the data set comprised of vacancies of each inequivalent oxygen position and interstitial oxygen atom at the O5 position (see Fig. 1). The approximate TSs were generated as the mid point between the defect free structure (initial) and the O1v-O5i, O2v-O5i, O4v-O5i FPs (final states), and between the O4v-O5i FP (initial state) and the O2v-O5i, O3v-O5i FPs (final states). Random perturbations of atomic positions and lattice vectors were applied to increase configurational diversity. These FPs and TSs were selected based on physical intuition of the most likely diffusion paths for oxygen atoms. Input structures were modified with the atomistic simulation environment (ASE)[72] and Atomsk[73].

Computational details of the DFT training set and validation calculations

All DFT calculations were carried out with the Vienna Ab Initio Simulation Package (VASP)[74–76] with the projector-augmented wave (PAW) method[77,78] and the generalized-gradient approximation of Perdew, Burke, and Ernzerhof (PBE)[79]. Spin polarization was neglected. The plane-wave energy cutoff was set to 600 eV, while sampling the Brillouin zone with a Gamma-centered Monkhorst-Pack[80] 2 × 2 × 1 k-mesh, corresponding to k-spacings below 0.09 $Å^{-1}$ in all cases. These computational parameters ensure an error below 4 meV/atom compared to a calculation with an 800 eV energy cutoff and a 4 × 4 × 2 k-mesh, while keeping the computational effort for dataset construction feasible. Convergence thresholds were set to 10^{-5} eV in energy for the self-consistent electronic minimization, and to 0.01 eV/Å on forces for structural relaxations. Gaussian smearing of 0.05 eV was applied to the electronic states to improve convergence.

Single-point calculations were carried out for configurations with atomic displacements in the defect-free case and for configurations with vacancies, interstitials, FPs, and TSs. Defect-free structures over a wide volume range were relaxed under fixed volume. Minimum energy paths for the formation of oxygen FPs were calculated with the climbing image nudged elastic bands (NEB) method[81,82] using 5 intermediate configurations along the diffusion path, with the same energy and force thresholds.

Parameters of the ACE potential

The final potential consists of 1000 functions per element, with a 7 Å cutoff radius for interaction with neighbors. We employed default parameters as implemented in pacemaker[59,83], using simplified Bessel radial functions, the Finnis-Sinclair embedding function, and applying an energy-based weighting policy on the training set, disregarding configurations with forces larger than 25 eV/Å. We also included the automatic core repulsion based on the ZBL potential[71]. All energies are shifted with reference to the isolated atoms, which were calculated with non-spin polarized DFT using a large box (edges of 30 Å). We tested alternative radial functions (exponentially-scaled Chebyshev polynomials) and increased the number of functions to 1400 per element, but observed no improvement in RMSEs or equation of state results. The chosen potential parameters, therefore, ensure accuracy and computational efficiency.

Computational details of calculations and molecular dynamics simulations with interatomic potentials

All calculations with the ACE and B+C potentials were carried out using LAMMPS[84]. Structural relaxations for equation of state and NEB calculations were carried out using a threshold for convergence on forces of 0.01 eV/Å.

The equation of state for the ACE potential was calculated using ASE[72] relaxing atomic positions and lattice vectors at each volume, whereas for the B + C potential, we employed LAMMPS and carried out structural relaxations at finite pressures. The unit cell was used for these calculations.

The NPT simulations employed a Nosé–Hoover thermostat and barostat with damping times of 0.05 and 1 ps, respectively, using a 1 fs timestep. All simulations employed the 0 K relaxed orthorhombic structure as the initial configuration. Simulated time ranged between 1.6 ns and 75 ns, depending on convergence of the a and b lattice parameters (see Supplementary Fig. 3). Lattice parameters were averaged over the last 1.5 ns of each simulation with values recorded every 10 fs. Analysis of the O site occupation was carried out with OVITO[70].

The SRO parameter for shell i is defined as:

$$SRO_i = 1 - \frac{n_i}{m_v c_i}, \tag{1}$$

where n_i is the number of unoccupied sites among c_i neighbors in the shell, and m_v is the concentration of unoccupied sites.

Data availability

The ACE potential, training dataset, and input files generated during this study are available in the Zenodo repository,https://doi.org/10.5281/zenodo.17249868.

Received: 18 December 2025; Accepted: 30 April 2026;

References

1. Coombs, T. A. et al. High-temperature superconductors and their large-scale applications. *Nat. Rev. Electr. Eng.* **1**, 788–801 (2024).
2. Obradors, X. & Puig, T. Coated conductors for power applications: materials challenges. *Supercond. Sci. Technol.* **27**, 044003 (2014).
3. MacManus-Driscoll, J. L. & Wimbush, S. C. Processing and application of high-temperature superconducting coated conductors. *Nat. Rev. Mater.* **6**, 587–604 (2021).
4. Sorbom, B. N. et al. ARC: a compact, high-field, fusion nuclear science facility and demonstration power plant with demountable magnets. *Fusion Eng. Des.* **100**, 378–405 (2015).
5. Vieira, R. F. et al. Design, fabrication, and assembly of the SPARC toroidal field model coil. *IEEE Trans. Appl. Supercond.* **34**, 0600615 (2024).
6. Kingham, D. & Gryaznevich, M. The spherical tokamak path to fusion power: opportunities and challenges for development via public-private partnerships. *Phys. Plasmas* **31**, 042507 (2024).
7. Meschini, S. et al. Review of commercial nuclear fusion projects. *Front. Energy Res*. https://doi.org/10.3389/fenrg.2023.1157394/full (2023).
8. Li, Z. Y. et al. Development and construction of magnet system for world's first full high temperature superconducting tokamak. *Superconductivity* **12**, 100137 (2024).
9. Sarasola, X. et al. Progress in the design of a hybrid HTS-Nb3Sn-NbTi central solenoid for the EU demo. *IEEE Trans. Appl. Supercond.* **30**, 1–5 (2020).
10. Federici, G. et al. Relationship between magnetic field and tokamak size—a system engineering perspective and implications to fusion development. *Nucl. Fusion* **64**, 036025 (2024).
11. Bottura, L. et al. Magnets for a muon collider—needs and plans. *IEEE Trans. Appl. Supercond.* **34**, 1–8 (2024).
12. Mariotto, S. et al. Study of HTS energy-saving superconducting magnet options for the PSI particle beam lines. *IEEE Trans. Appl. Supercond.* **35**, 1–5 (2025).
13. Giannini, L. et al. Advances in magnet and shielding designs for fusion and high energy physics applications. *Fusion Eng. Des.* **214**, 114899 (2025).
14. Omori, N. E., Bobitan, A. D., Vamvakeros, A., Beale, A. M. & Jacques, S. D. M. Recent developments in X-ray diffraction/scattering computed tomography for materials science. *Philos. Trans. R. Soc. A* **381**, 20220350 (2023).
15. Wang, Z. et al. Unraveling working and degradation mechanisms of energy storage and conversion materials at the nanoscale using synchrotron X-ray characterizations. *Adv. Mater.* **38**, e72655 (2026).
16. Park, S., Jeong, Y.-H. & Yu, Y.-S. A concise review of advances in X-ray spectromicroscopy and ptychography: applications in emerging energy materials. *Korean J. Chem. Eng.* **43**, 43–55 (2026).
17. Magdy, M. A brief account of the technology significance of synchrotron radiation: a state-of-the-art angle-resolved photoemission spectroscopy (ARPES). *Curr. Anal. Chem.* **22**, 771–778 (2026).
18. Dong, Z. et al. Sub-nanometer depth resolution and single dopant visualization achieved by tilt-coupled multislice electron ptychography. *Nat. Commun.* **16**, 1219 (2025).
19. Suh, W., Choi, J. B., Park, K.-Y. & Chang, C. S. Development of electron ptychography from algorithms, detectors to its applications. *Appl. Microsc.* **55**, 13 (2025).
20. Bednorz, J. G. & Müller, K. A. Possible high T_c superconductivity in the Ba–La–Cu–O system. *Z. Phys. B* **64**, 189–193 (1986).
21. Tsuei, C. C. & Kirtley, J. R. Pairing symmetry in cuprate superconductors. *Rev. Mod. Phys.* **72**, 969–1016 (2000).
22. Taillefer, L. Scattering and pairing in cuprate superconductors. *Annu. Rev. Condens. Matter Phys.* **1**, 51–70 (2010).

23. Norman, M. R. The challenge of unconventional superconductivity. *Science* **332**, 196–200 (2011).
24. Scalapino, D. J. A common thread: the pairing interaction for unconventional superconductors. *Rev. Mod. Phys.* **84**, 1383–1417 (2012).
25. Stewart, G. R. Unconventional superconductivity. *Adv. Phys.* **66**, 75–196 (2017).
26. Anderson, Z. W. et al. Gapped commensurate antiferromagnetic response in a strongly underdoped model cuprate superconductor. *npj Quantum Mater.* **10**, 93 (2025).
27. Oliviero, V. et al. Charge order near the antiferromagnetic quantum critical point in the trilayer high T_c cuprate $HgBa_2Ca_2Cu_3O_{8+\delta}$. *npj Quantum Mater.* **9**, 75 (2024).
28. Christos, M. & Sachdev, S. Emergence of nodal Bogoliubov quasiparticles across the transition from the pseudogap metal to the d-wave superconductor. *npj Quantum Mater.* **9**, 4 (2024).
29. Tallon, J. L. Oxygen in high-Tc cuprate superconductors. In (ed Narlikar, A. V.) *Frontiers in Superconducting Materials*, pp 295–330 https://doi.org/10.1007/3-540-27294-1_7 (Springer, Berlin, Heidelberg, 2005).
30. Johnson, C. L., Bording, J. K. & Zhu, Y. Structural inhomogeneity and twinning in $YBa_2Cu_3O_{7-\delta}$ superconductors: high-resolution transmission electron microscopy measurements. *Phys. Rev. B* **78**, 014517 (2008).
31. Borovik, A. S., Malyshevsky, V. S. & Rahimov, S. V. Ion channeling investigation of oxygen sublattice in $YBa_2Cu_3O_7$ crystal film. *Nucl. Instrum. Methods Phys. Res. B* **226**, 385–391 (2004).
32. Balatsky, A. V., Vekhter, I. & Zhu, J.-X. Impurity-induced states in conventional and unconventional superconductors. *Rev. Mod. Phys.* **78**, 373–433 (2006).
33. Feighan, J. P. F., Kursumovic, A. & MacManus-Driscoll, J. L. Materials design for artificial pinning centres in superconductor PLD coated conductors. *Supercond. Sci. Technol.* **30**, 123001 (2017).
34. Obradors, X. & Puig, T. Pin the vortex on the superconductor. *Nat. Mater.* **23**, 1311–1312 (2024).
35. Puig, T., Gutierrez, J. & Obradors, X. Impact of high growth rates on the microstructure and vortex pinning of high-temperature superconducting coated conductors. *Nat. Rev. Phys.* **6**, 132–148 (2024).
36. Ruiz, H. S. et al. Critical current density in advanced superconductors. *Prog. Mater. Sci.* **155**, 101492 (2026).
37. Nücker, N., Fink, J., Fuggle, J. C., Durham, P. J. & Temmerman, W. M. Evidence for holes on oxygen sites in the high-T_c superconductors $La_{2-x}Sr_xCuO_4$ and $YBa_2Cu_3O_{7-y}$. *Phys. Rev. B* **37**, 5158–5163 (1988).
38. Arpaia, R. et al. Dynamical charge density fluctuations pervading the phase diagram of a Cu-based high-T_c superconductor. *Science* **365**, 906–910 (2019).
39. Legris, A., Rullier-Albenque, F., Radeva, E. & Lejay, P. Effects of electron irradiation on $YBa_2Cu_30_{7-\delta}$ superconductor. *J. Phys. I* **3**, 1605–1615 (1993).
40. Unterrainer, R., Fischer, D. X., Lorenz, A. & Eisterer, M. Recovering the performance of irradiated high-temperature superconductors for use in fusion magnets. *Supercond. Sci. Technol.* **35**, 04LT01 (2022).
41. Unterrainer, R. et al. Responsibility of small defects for the low radiation tolerance of coated conductors. *Supercond. Sci. Technol.* **37**, 105008 (2024).
42. Fischer, D. X. et al. Influence of irradiation temperature on REBCO tape degradation. *Supercond. Sci. Technol.* **38**, 055019 (2025).
43. Mundet, B. et al. Local strain-driven migration of oxygen vacancies to apical sites in $YBa_2Cu_3O_{7-x}$. *Nanoscale* **12**, 5922–5931 (2020).
44. Torsello, D. et al. Radiation environment and damage of HTS magnets in an ARC-like reactor. *IEEE Trans. Appl. Supercond.* **35**, 1–6 (2025).
45. Torsello, D., Gambino, D., Gozzelino, L., Trotta, A. & Laviano, F. Expected radiation environment and damage for YBCO tapes in compact fusion reactors. *Supercond. Sci. Technol.* **36**, 014003 (2023).
46. Torsello, D. et al. Roadmap for the investigation of irradiation effects in HTS for fusion. *Supercond. Sci. Technol.* **38**, 053501 (2025).
47. Jorgensen, J. D. et al. Oxygen ordering and the orthorhombic-to-tetragonal phase transition in $YBa_2Cu_3O_{7-x}$. *Phys. Rev. B* **36**, 3608–3616 (1987).
48. Schuller, I. K. et al. Structural phase transition in $YBa_2Cu_3O_{7-\delta}$: the role of dimensionality for high temperature superconductivity. *Solid State Commun.* **63**, 385–388 (1987).
49. Bonetti, E., Campari, E. G., Mattioli, P. & Zingaro, A. Stoichiometry dependence of oxygen anelastic relaxation in $YBa_2Cu_3O_{7-x}$ and the orthorhombic-to-tetragonal phase transition. *J. Alloy. Compd.* **211-212**, 314–317 (1994).
50. Chaplot, S. L. Molecular-dynamics simulation of $YBa_2Cu_3O_7$ at high temperatures. *Phase Transit.* **19**, 49–59 (1989).
51. Chaplot, S. L. Phonon dispersion relation in $YBa_2Cu_3O_7$. *Phys. Rev. B* **37**, 7435–7442 (1988).
52. Chaplot, S. L. Interatomic potential, phonon spectrum, and molecular-dynamics simulation up to 1300 K in $YBa_2Cu_3O_{7-\delta}$. *Phys. Rev. B* **42**, 2149–2154 (1990).
53. Gray, R. L., Rushton, M. J. D. & Murphy, S. T. Molecular dynamics simulations of radiation damage in $YBa_2Cu_3O_7$. *Supercond. Sci. Technol.* **35**, 035010 (2022).
54. Dickson, A., Gilbert, M. R., Nguyen-Manh, D. & Murphy, S. T. Threshold displacement energies of oxygen in $YBa_2Cu_3O_7$: a multi-physics analysis. *J. Nucl. Mater.* **618**, 156239 (2026).
55. Behler, J. Perspective: Machine learning potentials for atomistic simulations. *J. Chem. Phys.* **145**, 170901 (2016).
56. Friederich, P., Häse, F., Proppe, J. & Aspuru-Guzik, A. Machine-learned potentials for next-generation matter simulations. *Nat. Mater.* **20**, 750–761 (2021).
57. Mishin, Y. Machine-learning interatomic potentials for materials science. *Acta Mater.* **214**, 116980 (2021).
58. Deringer, V. L., Caro, M. A. & Csányi, G. Machine learning interatomic potentials as emerging tools for materials science. *Adv. Mater.* **31**, 1902765 (2019).
59. Bochkarev, A. et al. Efficient parametrization of the atomic cluster expansion. *Phys. Rev. Mater.* **6**, 013804 (2022).
60. Loutati, A., Sohn, Y. J. & Tietz, F. Phase-field determination of NaSICON materials in the quaternary system Na_2O-P_2O_5-SiO_2-ZrO_2: the series $Na_3Zr_{3-x}Si_2P_xO_{11.5+x/2}$. *ChemPhysChem* **22**, 995–1007 (2021).
61. Attarian, S., Morgan, D. & Szlufarska, I. Studies of Ni-Cr complexation in FLiBe molten salt using machine learning interatomic potentials. *J. Mol. Liq.* **400**, 124521 (2024).
62. Liu, J., Byggmästar, J., Fan, Z., Qian, P. & Su, Y. Large-scale machine-learning molecular dynamics simulation of primary radiation damage in tungsten. *Phys. Rev. B* **108**, 054312 (2023).
63. Leimeroth, N., Rohrer, J. & Albe, K. General purpose potential for glassy and crystalline phases of Cu-Zr alloys based on the ACE formalism. *Phys. Rev. Mater.* **8**, 043602 (2024).
64. Liu, Y., He, X. & Mo, Y. Discrepancies and error evaluation metrics for machine learning interatomic potentials. *npj Comput. Mater.* **9**, 174 (2023).
65. Fellman, A., Byggmästar, J., Granberg, F., Nordlund, K. & Djurabekova, F. Fast and accurate machine-learned interatomic potentials for large-scale simulations of Cu, Al, and Ni. *Phys. Rev. Mater.* **9**, 053807 (2025).
66. Poul, M., Huber, L. & Neugebauer, J. Automated generation of structure datasets for machine learning potentials and alloys. *npj Comput. Mater.* **11**, 174 (2025).
67. Drautz, R. Atomic cluster expansion for accurate and transferable interatomic potentials. *Phys. Rev. B* **99**, 014104 (2019).
68. Drautz, R. Atomic cluster expansion of scalar, vectorial, and tensorial properties including magnetism and charge transfer. *Phys. Rev. B* **102**, 024104 (2020).
69. Cowley, J. M. An approximate theory of order in alloys. *Phys. Rev.* **77**, 669–675 (1950).

70. Stukowski, A. Visualization and analysis of atomistic simulation data with OVITO—the Open Visualization Tool. *Modell. Simul. Mater. Sci. Eng.* **18**, 015012 (2009).
71. Ziegler, J. F. & Biersack, J. P. *The Stopping and Range of Ions in Matter*, pp 93–129 https://doi.org/10.1007/978-1-4615-8103-1_3. (Springer US, Boston, MA, 1985).
72. Hjorth Larsen, A. et al. The atomic simulation environment—a Python library for working with atoms. *J. Phys.* **29**, 273002 (2017).
73. Hirel, P. Atomsk: a tool for manipulating and converting atomic data files. *Comput. Phys. Commun.* **197**, 212–219 (2015).
74. Kresse, G. & Hafner, J. Ab initio molecular dynamics for liquid metals. *Phys. Rev. B* **47**, 558–561 (1993).
75. Kresse, G. & Furthmüller, J. Efficiency of ab-initio total energy calculations for metals and semiconductors using a plane-wave basis set. *Comput. Mater. Sci.* **6**, 15 – 50 (1996).
76. Kresse, G. & Furthmüller, J. Efficient iterative schemes for ab initio total-energy calculations using a plane-wave basis set. *Phys. Rev. B* **54**, 11169–11186 (1996).
77. Blöchl, P. E. Projector augmented-wave method. *Phys. Rev. B* **50**, 17953–17979 (1994).
78. Kresse, G. & Joubert, D. From ultrasoft pseudopotentials to the projector augmented-wave method. *Phys. Rev. B* **59**, 1758–1775 (1999).
79. Perdew, J. P., Burke, K. & Ernzerhof, M. Generalized gradient approximation made simple. *Phys. Rev. Lett.* **77**, 3865–3868 (1996).
80. Monkhorst, H. J. & Pack, J. D. Special points for Brillouin-zone integrations. *Phys. Rev. B* **13**, 5188–5192 (1976).
81. Henkelman, G., Uberuaga, B. P. & Jónsson, H. A climbing image nudged elastic band method for finding saddle points and minimum energy paths. *J. Chem. Phys.* **113**, 9901–9904 (2000).
82. Henkelman, G. & Jónsson, H. Improved tangent estimate in the nudged elastic band method for finding minimum energy paths and saddle points. *J. Chem. Phys.* **113**, 9978–9985 (2000).
83. Lysogorskiy, Y. et al. Performant implementation of the atomic cluster expansion (PACE) and application to copper and silicon. *npj Comput. Mater.* **7**, 1–12 (2021).
84. Thompson, A. P. et al. LAMMPS—a flexible simulation tool for particle-based materials modeling at the atomic, meso, and continuum scales. *Comput. Phys. Commun.* **271**, 108171 (2022).

Acknowledgements

The computations were enabled by resources provided by the National Academic Infrastructure for Supercomputing in Sweden (NAISS) at the National Supercomputer Center (NSC), Linköping University, and at the PDC Center for High Performance Computing, KTH Royal Institute of Technology, partially funded by the Swedish Research Council through Grant Agreement No. 2022-06725. DG acknowledges financial support from the Swedish Research Council (VR) through Grant No. 2023-00208. NDE acknowledges that this publication is part of the project PNRR-NGEU, which has received funding from the MUR—DM 117/2023 (or DM 118/2023). N.D.E., D.T., and F.L. acknowledge support from Eni S.p.A. J.B. acknowledges funding from the Research Council of Finland through the OCRAMLIP project, grant number 354234. F.D. acknowledges the Research Council of Finland project SPATEC (Grant No 349690) for financial support.

Author contributions

D.G., D.T., and F.L. conceived the project. D.G. and N.DE. carried out all the simulations. J.B. assisted with the creation of the data set and the training of the potential. J.K. and F.D. contributed to the identification of the simulation methodology. All authors contributed to the interpretation of the results and the writing of the manuscript.

Funding

Open access funding provided by Linköping University.

Competing interests

The authors declare no competing interests.

Additional information

Supplementary information The online version contains supplementary material available at https://doi.org/10.1038/s41535-026-00891-7.

Correspondence and requests for materials should be addressed to Davide Gambino.

Reprints and permissions information is available at http://www.nature.com/reprints